Tomographic Microscopy of Functionally Graded Polymer-Derived SiCN Ceramics with Tunable Gradients

Lorenz Hagelüken[1], Malgorzata Grazyna Makowska[2], Federica Marone[2], and Juergen Brugger[1*]

[1]*Microsystems Laboratory, Ecole Polytechnique Fédérale de Lausanne, 1015 Lausanne, Switzerland*
[2]*Swiss Light Source, Paul Scherrer Institute, 5232 Villigen, Switzerland*
[*]*E-mail: juergen.brugger@epfl.ch*

Abstract

Polymer-derived ceramics (PDCs) are a very attractive class of materials due to their excellent properties such as resistance to high temperatures and harsh environments, adjustability of mechanical and functional behavior, and compatibility with a broad range of shaping techniques. The liquid nature of the silicon-containing polymeric precursors and the composition tuning via addition of fillers set the stage for the creation of functionally graded ceramics (FGCs). Polysilazane-based precursors with and without divinylbenzene (DVB) addition for carbon concentration increase are sequentially cast in three different custom molds. DVB concentration, casting order, and thermal processing conditions are varied to study their influence on the interface nature and composition gradient of the functionally graded ceramic parts which are obtained after pyrolysis at 1000–1400 °C. Synchrotron-based tomographic microscopy was applied for high-resolution 3D visualization of the parts, allowing clear distinction of the dissimilar regions and approximate quantification of the composition gradients tunable from submicrometer to millimeter transition lengths. Achieving spatially defined electrical conductivity contrasts in monolithic silicon carbonitride parts, an LED attached onto a FGC plate outlines a promising use case for harsh environment applications.

Fig. 0: Graphical abstract.
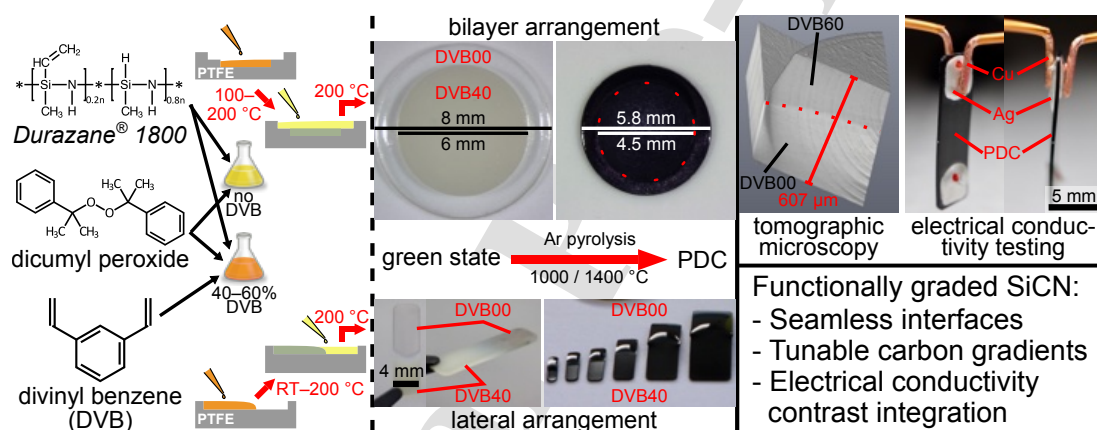
1 Keywords

Polymer-derived ceramics, Functionally graded materials, Functionally graded ceramics, Molding, Tomographic microscopy

1 Introduction

Polymer-derived ceramics (PDCs) such as silicon carbonitride (SiCN) exhibit a unique set of properties including resistance to high temperatures and harsh environments, property tunability, and compatibility with a broad range of shaping techniques [1]. Mastery of these three aspects would ultimately allow for advanced PDC-based applications in harsh environments. In addition to homogeneous inert elements as passive [2] or sensing [3] material, engineering of property gradients in PDC parts could render complex functionality integration possible where otherwise ceramic-ceramic or metal-ceramic joining is common yet prone to failure due to atomic bonding differences or mismatching coefficient of thermal expansion (CTE) [4]. These so-called functionally graded materials (FGMs) or more specifically functionally graded ceramics (FGCs) are defined as volumes with a continuous, stepped, or spatial change in composition and / or microstructure [5,6].

A conventional approach for harsh environment monolithic devices is co-fired ceramics where green tapes are patterned, filled with metallic pastes, and laminated. Categorized in high-temperature (HTCCs, >1000 °C) and low-temperature co-fired ceramics (LTCCs, <1000 °C), suited materials like high-melting (e.g. platinum) or lower temperature melting metals (e.g. silver) and glassy phases, respectively, are applied [7]. However, involved noble metals are expensive, co-fired ceramics are also constraint by mismatched CTEs [8] and especially LTCCs have limited operating temperatures. Mismatching CTEs and resulting stress is also the major challenge of metal-ceramic joining in processes such as brazing [9]. Recently, advances in additive manufacturing (AM) facilitated new arrangements and applications [5]. For instance, copper has been integrated into a kaolin ceramic matrix by a multi-vat digital light processing (DLP) technique. 3D freeform electrical paths were spatially defined within the otherwise insulating part, supplying an LED with power [10].

Overcoming poor thermomechanical properties of ceramic-ceramic assemblies joined by brazing or diffusion bonding [9], silicon-containing preceramic polymers (PCPs) were investigated as liquid

3

28 adhesive. Colombo et al. joined silicon carbide with a thin layer of a siloxane-based solution [11] and

29 according to their findings, the use of low heating rates is recommended [12]. Further examples using

30 polysiloxanes [13], polycarbosilanes [14], or polysilazanes [15] as adhesive have been demonstrated

31 for SiAlCN, SiC, or copper/epoxy molding compound composite to be joined. Strength of the obtained

32 joints is in the order of other joining techniques and often is more temperature resistant. Compared

33 to the bulk material, however, joints typically are the weak point. This problem was overcome for

34 PDCs by the "polymer-based bonding" technique, presented by An et al. [16] and Liew et al. [17,18]

35 in 2000/2001. Joining the parts in the organic green state before pyrolysis, using the same liquid

36 PCP (formulation) the green parts were derived from, established crosslinking across the parts. This

37 process, yielded neither noticeable defects nor any noticeable interface after pyrolysis.

38 Two major advantages of PDCs are their great compatibility with various shaping techniques and

39 the adjustability of their properties. Extensive efforts have been invested in the investigation of tech-

40 niques benefiting from the liquid nature of the precursor, e.g. fiber drawing, coating, casting, or

41 additive manufacturing [16,19–22]. Many groups studied the influences of precursor class, filler ad-

42 dition, processing route, and thermal as well as atmospheric processing parameters on the ceramics'

43 composition, microstructure, and mechanical and functional properties [23–30]. Tuning of PDCs'

44 electrical conductivity is mainly achieved by the addition of metallic or carbon (C) fillers. Several

45 metals were used as conducting phase, introduced in the form of metal salts or complexes including

46 for example titanium [31,32], or copper, nickel, and cobalt [33,34]. More commonly, carbon-fillers

47 are added. Divinylbenzene (DVB) is cost-efficient and conveniently mixes and cross-polymerizes with

48 the PCP [35–38] but several carbon allotropes such as carbon nanotubes (CNTs) and graphene have

49 been demonstrated to significantly increase the PDC's electrical conductivity as well [39–43]. De-

50 pending on the carbon concentration and distribution, the dc conductivity at room-temperature (RT)

51 ranges across up to 15 orders of magnitude (typically $\sim 10^{-10}$–1 S/cm) [1,44], recent observation of

52 "abnormal graphitization in near-surface/ interface regions" locally yielded values up to 14 S/cm [45].

53 The increased occurrence near the surfaces was observed not only in the case of carbon, but also in

54 case of titanium-filled silicon oxycarbide [32].

55 The graded structure of FGMs allows for unique combinations of properties that cannot be achieved

4

56 with monolithic composites[46]. Few examples of functionally graded PDCs have been reported so

57 far. One class is concerned with the creation of a porosity gradient by controlled bubble nucleation

58 and viscosity increase dynamics or a temperature gradient during thermal curing [47–50]. Diode

59 functionality based on a p-n-junction has been demonstrated by combining a p-type SiCNO and an n-

60 type SiBCNO [51,52]. A continuous ceramic-to-polymer gradient composite has been manufactured

61 by dissimilar thermal processing of a green state bar in a custom-designed heating and cooling sys-

62 tem [53]. A PDC-based double-layer thermistor has been developed by combination of a DVB-filled

63 SiCN sensing element onto an unfilled SiCN serving as substrate [38]. Lamination of several partially

64 crosslinked PCP tapes filled with small or large silicon carbide particles followed by pressure-assisted

65 thermal processing yielded functionally graded ceramic matrix composites with adjustable mechanical

66 properties [54].

67 Making use of the liquid nature of the precursors as well as the ability to tune the ceramic compo-

68 sition and electrical conductivity by addition of DVB, functionally graded PDCs with an engineered

69 contrast and functionality integration are presented in this work. Geometrically defined combination

70 of organopolysilazane-based PCP formulations with and without DVB in an early stage of the process-

71 ing route followed by joint thermal treatment yields monolithic SiCN parts, in which a slight contrast

72 in atomic composition and microstructure results in a conductivity contrast of 5–10 orders of magni-

73 tude while otherwise behaving very similarly in terms of material properties. This contrast is due to

74 the segregated free carbon occurrence and microstructure which represents the only conducting phase

75 in the material at RT [44]. The influence of the casting order and thermal processing parameters on

76 the interface nature is investigated by means of scanning electron microscopy (SEM), transmission

77 electron microscopy (TEM), and synchrotron-based tomographic microscopy, allowing for a high-

78 resolution 3D visualization of the FGCs. As a sample application, an SiCN plate with two electrically

79 conducting feedthroughs seamlessly integrated into an insulating matrix is presented which supplies

80 a light-emitting diode (LED) with power. This technique reduces time and effort for ceramic join-

81 ing or assembly as well as the risk of failure. Considering the excellent properties of PDCs and the

82 PDC route's compatibility with several advanced shaping techniques, functionally graded PDCs are

83 a promising approach for applications in chemical engineering, energy conversion, and biomedical

5

84 implants.

2 Materials and methods

2.1 Synthesis of functionally graded SiCN Ceramics

87 The functionally graded ceramic samples were fabricated by molding in CNC-machined polytetraflu-

88 oroethylene (PTFE). For successful green part / body (GB) mold release, the mold surface finish is

89 essential, the areal roughness (Sq / Sa) should be in the order of 5 μm or better. The dissimilar PCP

90 formulations were sequentially cast, normally with an intermediate thermal (pre-)curing step (Fig-

91 ure S1b). The mold geometry for the first type of contrast samples is shown in Figure S2a. These

92 molds consist of two cylindrical layers with diameters of 6 and 8 mm and a depth of 500 μm each.

93 Eight of them are combined in one mold array. One or several of these PTFE mold arrays were placed

94 on the level hotplate inside the argon (Ar) glovebox. The general material processing is based on our

95 previous work [55] which among other results reports mechanical and electrical properties as well as

96 compositional data also relevant to this current work. The modified fabrication process of the current

97 work is outlined in Figure 1. The casting and thermal curing sequences and volumes are provided

98 in Table 1. The DVB-filled PCP formulation (3% dicumyl peroxide (DCP), typically 60% DVB),

99 19.8 μL ($\equiv$140%[1] of the layer's volume) was first pipetted into each molds' lower layer and thermally

100 cured. When cooled down to RT, the DVB-unfilled PCP was cast and jointly crosslinked. Nomencla-

101 ture of the contrast samples is based on the casting order, these samples will therefore be referred to

102 as DVB60|00 bilayer in the following. In case of the opposite casting order (DVB00|60), the DVB-

103 free PCP was cast into the molds' lower layers and extensively thermally cured. The DVB containing

104 PCP (typically 60%) was then pipetted on top and cured in a 3-step sequence of 10 min each at 100,

105 150, and 200 °C. For demolding, molds were generally flipped upside down and gently tapped. PTFE

106 molds were immersed in acetone, brushed, rinsed with IPA, and dried before reuse.

107 The second graded sample type are rectangular bars with aspect ratios (AR) of 3.25≤AR≤4 in

108 which the dissimilar PCPs were arranged laterally (LHBs). Eight molds are combined in one array in

---

[1]PCP overfilling compensates for partial volatilization during thermal crosslinking and contributes to a more planar interface in DVB60|00 casting order. In the opposite DVB00|60 casting order, it was not done in case of the upper layer to prevent DVB60 overflow.
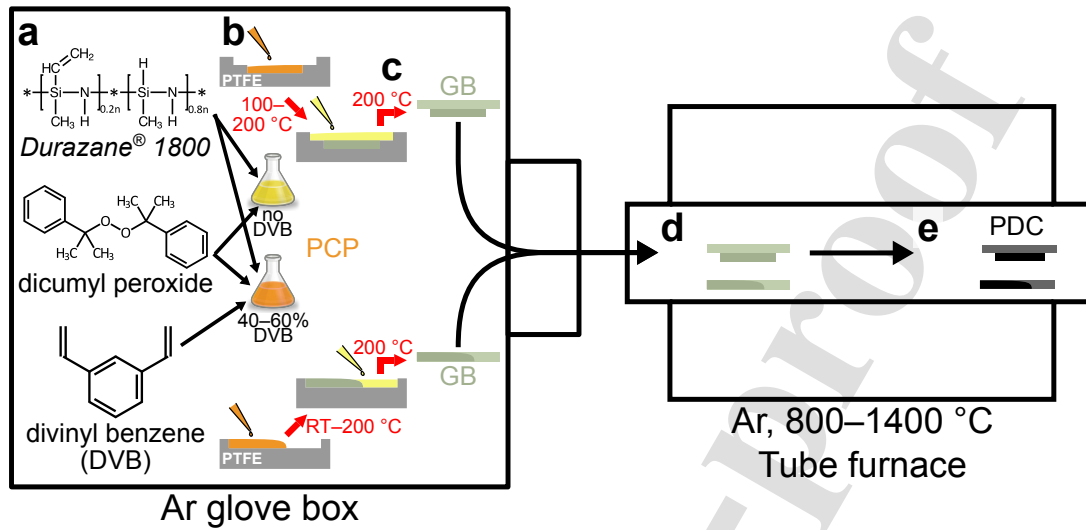
Fig. 1: Schematic of the PDC fabrication process in argon atmosphere: **a)** Preceramic polymer formulation; **b)** bilayer or lateral casting and thermal crosslinking; **c)** solidification and green body mold release; **d)** transfer into the tube furnace for pyrolysis; **e)** transformation to functionally graded PDCs.

Tab. 1: Nomenclature and fabrication details of functionally graded SiCN parts: Composition casting order, absolute volumes, relative filling with respect to the theoretical mold volume, and thermal curing conditions for bilayer, laterally heterogeneous bars, and bi-feedthrough geometry. *3S* abbreviates the standard 3-step curing sequence for DVB-filled precursors (10 min @ 100 °C + 10 min @ 150 °C + 10 min @ 200 °C).

Arrangement	Name	1st casting Volume (µL / %)	Thermal pre-curing	2nd casting Volume (µL / %)	Final curing
Bilayer	DVB60|00 (TEM)	DVB60 19.8 / 140	10 min @ 100 °C + 10 min @ 150 °C	DVB00 25.1 / 100	30 min @ 200 °C
	DVB60|00	DVB60 19.8 / 140	15 min @ 100 °C	DVB00 30.2 / 120	30 min @ 200 °C
	DVB00|60	DVB00 19.8 / 140	30 min @ 200 °C	DVB60 25.1 / 100	3S
LHB	**Std (T0)**: GB-L	DVB40 11.2 / 140	3S	DVB00 9.7 / 120	30 min @ 200 °C
	T2: GB-L	DVB00 9.7 / 120	5 min @ 200 °C	DVB40 9.7 / 120	3S
	T4: L/GB-L	DVB00 9.7 / 120	1 min @ 175 °C	DVB40 9.7 / 120	3S
	T5: L-L	DVB40 11.2 / 140	none	DVB00 9.7 / 120	20 min @ 150 °C + 10 min @ 200 °C
BFT	DVB40|00	DVB40 2× 18.0 / 130	3S (but 20 min @ 200 °C)	DVB00 275 / 74	20 min @ 180 °C + 10 min @ 200 °C

7

PTFE, shown in Figure S2b. They are 500 μm deep, have corner radii of 1 mm and six different sizes with lateral dimensions of 8×2, 9.5×2.5, 11×3, 14×4, 20×6 and 26×8 mm^2, of which only 11×3 mm^2 is used in the following. As illustrated in the Figure 1, the first PCP formulation was pipetted into one end of the cavity, followed by a thermal intermediate pre-curing step, pipetting of the dissimilar precursor into the mold's opposite end, and a joint final curing step. Sequence, volumes, and thermal treatments indicating the decreasing extent of thermal pre-curing from type 0 (standard: green body-liquid joining) to type 5 (liquid-liquid joining) are shown in Table 1.

Composition-contrast ceramic bi-feedthrough (BFT) plates were fabricated using dedicated CNC-machined PTFE molds which consist of a square matrix of 20×20 mm^2 with a depth of 1 mm and corner radii of 2 mm. There are two 100 μm recessed circular areas of 4 mm diameter and 4 mm spacing which serve for placing the liquid inset PCP. One large droplet of the DVB 40 PCP was placed onto each recessed area. The volumes of 18 μL were chosen, in order to achieve the maximum material height with no or minimal lateral spreading exceeding the predefined area. To render the PCP droplets stable, they were thermally pre-cured before the dissimilar matrix PCP (DVB00) was cast around. The matrix volume of 275 μL was selected to not bury the green parts but leave the insets' top exposed. After joint thermal curing and thermosetting of the matrix, BFT green parts were released from the mold by upside down tapping at elevated temperatures around 100 °C.

The composition-contrast green parts were placed in Al$_2$O$_3$ crucibles for Ar atmosphere pyrolysis. Bilayer samples were processed at heating and cooling rates of 100 K/h and peak temperatures of 1000 and 1400 °C (Figure S3: solid lines). The seven types of laterally graded bars and BFT plates were pyrolyzed at 1000 and 1400 °C as shown in Figure S4a,c. In this case, pyrolysis parameters were optimized with a reduced heating rate of 60 K/h in the temperature range of 300–800 °C (Figure S3: dotted lines), resulting in low scrap rates of 0% for 1000 °C and 14% for 1400 °C pyrolysis (Figure S4b,d).

2.2 Characterization

The cross sections of some samples were prepared by means of cleaving or diamond-wire sawing. Part inspection and imaging were performed by optical microscopy (OM; M80, Leica, Germany;

8

136 Eclipse L200, Nikon, Japan) and SEM (Merlin, Zeiss, Germany). The electrical conductivity was

137 measured in a 2-probe bulk approach in transition. A custom two-probe setup was built where the

138 probes were connected to a Keithley 2400 source meter. In order to ensure a good electrical contact,

139 the Cu probe tips were polished and a conductive two-component Ag epoxy glue (Epo-Tek® H20E,

140 Epoxy Technology, United States) was applied on both sides of the PDC discs to be measured. The

141 Ag glue was placed centered and spread to cover a circular area with 80% of the specimens's diameter.

142 Samples were clamped between the probes for measurement and then flipped and recontacted for a

143 second measurement. Resistance R was obtained as the inverse of the IV-curve linear regression

144 line, IV ranges were adapted depending on the samples' conductivity and kept well below values

145 which would cause heat induced effects. Based on Pouillet's law (Equation 1, with t for the specimen

146 thickness and A for the effective cross-sectional area), the conductivity σ_{dc} was finally calculated

147 in good approximation through rearrangement and calculation of the approxiamative specimen area

148 based on the silver epoxy contact diameter d_{Ag} (Equation 2):

$$R = \rho \frac{t}{A} \tag{1}$$

149

$$\sigma_{dc} = \rho^{-1} = \frac{t}{RA} = \frac{t}{R\pi \left(\frac{d_{Ag}}{2}\right)^2} = \frac{4t}{R\pi(d_{Ag})^2} \tag{2}$$

150 Preparation for TEM analysis of a DVB60|00 1400 °C pyrolyzed bilayer sample (intermediate cur-

151 ing: 10 min at 100 °C, 10 min at 150 °C), involving 1 μm carbon sputtering and gallium (Ga+) FIB

152 lamella cutting, was performed with a NVision 40 (Zeiss, Germany). TEM, high-resolution trans-

153 mission electron microscopy (HRTEM), and energy-dispersive X-ray spectroscopy (EDX) were then

154 conducted on a Tecnai Osiris (FEI, United States).

155 Several bilayer and laterally heterogeneous SiCN samples were analyzed by means of X-ray ab-

156 sorption contrast tomographic microscopy. To achieve sufficient contrast between the dissimilar SiCN

157 regions, relatively low energy X-rays had to be used, which determined the dimensions of the spec-

158 imens to be in the range of a few hundreds of micrometers. For this reason, bilayer samples were

159 typically cleaved into small pieces. In case of the lateral composition-gradient bar samples, the ROI,

160 a sharp angle triangular center piece, was cut out of each sample (sized ~8.2×2.2 mm^2 resulting from

9

161 11×3 mm^2 molds) by diamond wire sawing (Figure S5). Microtomography was performed at PSI SLS

162 TOMCAT beamline [56]. The vertically mounted PDC samples were placed into the 12, 15 or 20 keV

163 X-ray beam and rotated by 180° around their long axis. Data was acquired with a detector system con-

164 sisting of a 20 μm thick LuAG:Ce scintillator, a 10× or 20× microscope lens, and an sCMOS camera.

165 These configurations result in a field of view of 1.66×1.4 mm^2 or 830×700 μm^2 and pixel sizes of 0.65

166 or 0.325 μm for 10× or 20× magnification, respectively. A gridrec algorithm [57] reconstructed to-

167 mographic volumes from the X-ray projections which were then visualized and analyzed using Avizo

168 software (Thermo Fischer, United States). In the case of T4, three adjacent scans were stitched.

3 Results and discussion

3.1 Microstructure of high-contrast graded SiCN

171 Comprehensive compositional and microstructure information at high resolution was first obtained for

172 one DVB60|00 bilayer sample (the lower DVB60 layer was pre-cured during 10 min at 100 °C and

173 10 min at 150 °C; 1400 °C pyrolyzed) which was prepared for SEM, EDX, and TEM. On the lamella,

174 a gray contrast is clearly visible in the SEM image in Figure 2a i. Thanks to a sensitive EDX detector

175 and high DVB-filling contrast (60|00), EDX mapping (Figure 2a ii) was able to visualize a significant

176 difference of carbon concentration between the (upper) filled and (lower) unfilled SiCN. An EDX

177 line scan was performed perpendicular to the interface. The carbon and silicon concentration profiles

178 shown in Figure 2a iii allow for an approximate quantification of the compositional transition length

179 which is in the order of 0.5 μm in this case with extended lower layer intermediate pre-curing.

180 The same DVB60|00-contrast lamella was then imaged by TEM. Several HRTEM images were

181 recorded in the interface region but within the field of view of 100×65 nm^2, no obvious change or

182 trend in the random glassy network microstructure could be observed in single images. Two examples

183 of HRTEM images from homogeneous regions are shown in Figure 2b. They originate from locations

184 approximately 2.5 μm away from the interface and exhibit features typical for SiCN processed at high

185 temperatures of 1400 °C. Both the unfilled (Figure 2b i) and DVB60-filled (Figure 2b ii) material

186 contain short-range structural features. Firstly, there are approximately 10 nm large dark crystallites

187 with an interplanar distance of 0.25 nm, corresponding to β-SiC's (111) d-spacing [35]. The planes

10

188 of this β-SiC cause the two diffraction rings with the relative high intensity in the selected area elec-

189 tron diffraction (SAED) patterns [58] which were recorded in thicker lamella regions in order not

190 to be impaired by possible beam amorphization effects. Secondly, both HRTEM images also show

191 ribbon-like features with interlayer spacings ranging from 0.34 up to 0.42 nm. These features are

192 turbostratic graphitic phases, also called basic structural units (BSUs). Comparing their occurrence

193 and structure between DVB00 and DVB60 SiCN, there are noticeably more and longer BSUs in the

194 DVB-filled material, which furthermore consist of more stacked layers. The selective addition of

195 DVB as a carbon-filler to the PCP therefore effectively altered the obtained SiCN's composition and

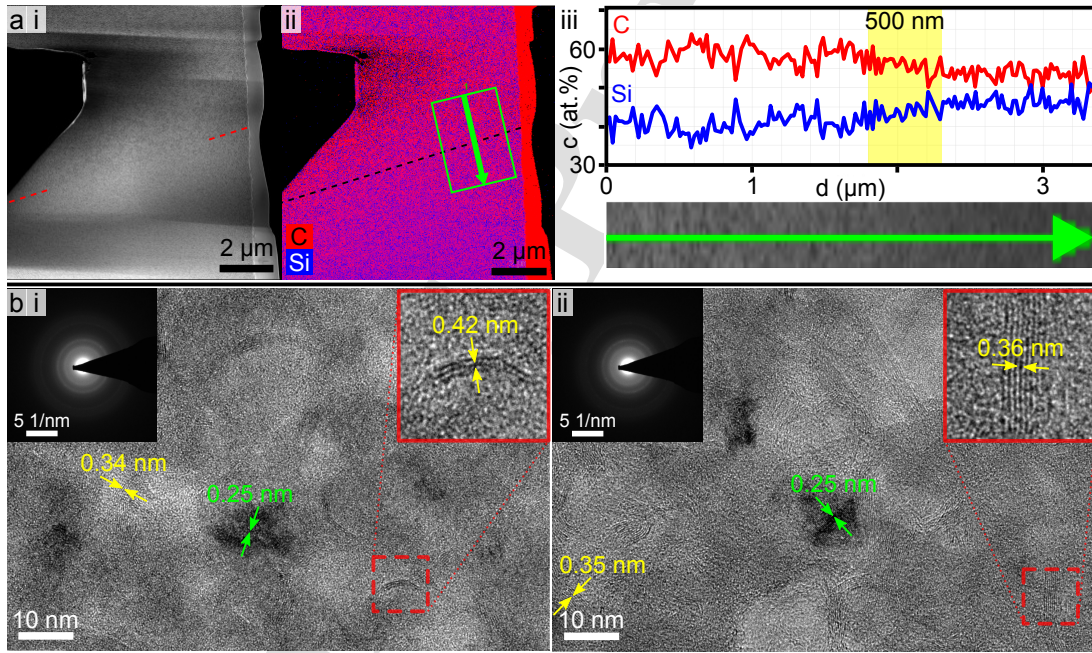196 microstructure, with spatial control in a monolithic sample.

Fig. 2: HRTEM analysis of 1400 °C pyrolyzed DVB60|00 bilayer sample FIB-cut into lamella: **a)** EDX analysis: **i)** SEM image with interface position highlighted in red; **ii)** C and Si EDX map with line scan positioning highlighted in green, perpendicular to interface line; **iii)** line scan EDX data showing a transition length of ∼500 nm; **b)** HRTEM images with SAED patterns: **i)** characteristic TEM image of DVB00 region with SiC precipitate and few C BSUs highlighted in green and yellow, respectively; **ii)** characteristic TEM image of DVB60 region with SiC precipitates and overall more C BSUs.

11

3.2 Influence of the casting order

Tomographic microscopy allows for high-resolution 3D visualization of entire sample volumes. Due to only slight difference in the chemical composition, X-ray attenuation coefficients of DVB-filled and unfilled ceramic regions are very similar, resulting in a very poor contrast. Using monochromatic and partially coherent synchrotron light allowed to obtain a sufficient contrast to distinguish the two materials. The obtained resolution allowed to resolve features of ~1 μm. Fabricated in the 6|8 mm bilayer PTFE molds, two samples with opposite casting orders were compared. In case of DVB60|00 order, the lower DVB60 layer was mildly pre-cured (partially crosslinked) during 15 min at 100 °C. In the opposite DVB00|60 arrangement, the lower DVB00 layer was extensively pre-cured during 30 min at 200 °C. The 3D reconstructed microtomography images of both sample types, cleaved into smaller pieces, are presented in Figure 3. For both casting orders (Figure 3a,d), the volumes are entirely free of cracks and pores, despite the high DVB-filling contrast and high pyrolysis temperature of 1400 °C. This indicates the suitability of the pressureless thermal crosslinking conditions and the applied heating and cooling rates of 100 K/h during pyrolysis. DVB as a crosslinker and carbon filler is generally advantageous in PDC processing due to enhanced hydrosilylation occurrence. Hydrosilylation is a favorable crosslinking mechanism forming strong Si-C-Si / Si-C-C-Si units which improve the mechanical strength, reduce outgassing and increase the ceramic yield and therefore help to obtain dense and crack-free ceramics [35,59]. Layered phase contrasts are clearly visible in Figure 3a,b,d,e. The interfaces are seamless and curved, convex in case of DVB00|60 due to lower layer overfilling and concave in case of DVB60|00. The latter curvature is the result of the PCP top layer curing first, followed by partial volatilization of the subjacent volume (mainly short oligomers and DVB molecules). In order to quantify and compare the SiCN composition gradients resulting from the sequential casting of DVB-filled and unfilled precursor, intensity profiles perpendicular to the interface were again evaluated (Figure 3b,c,e,f). The grayscale line profiles confirm the visual impression from the 3D and 2D views that the DVB60|00 order exhibits a smoother transition in this case. There are two possible reasons contributing to the ~25 μm long transition range. Firstly, DVB60 PCP has previously shown to typically form a rougher top surface [55] compared to DVB00 which results in a gradual change in the grayscale around the interface. Secondly, compared to the bilayer sample analyzed by TEM,

12

the lower DVB60 layer was pre-cured very mildly only. Thermal treatment during 15 min at 100 °C (compared to 10 min each at 100 and 150 °C) was apparently sufficient to consolidate the global shape (curved interface line) but possibly still allowed for interlayer mixing or DVB diffusion processes on the micro-scale. This indicates that the composition gradient in bilayer SiCN is adjustable by the variation of the pre-curing degree. The third example (DVB00|60 arrangement), where the lower layer was extensively thermally crosslinked (30 min at 200 °C) suggests a chemical influence of the casting order on the interface nature. Despite extensive pre-curing, it shows a transition length of ~5 μm (Figure 3e,f), in between the previous two values. In this case, the DVB molecules contained in the upper liquid precursor formulation potentially diffused into the DVB-free GB layer below before the second thermal curing step immobilized them by integration into the upper layer crosslinked network.
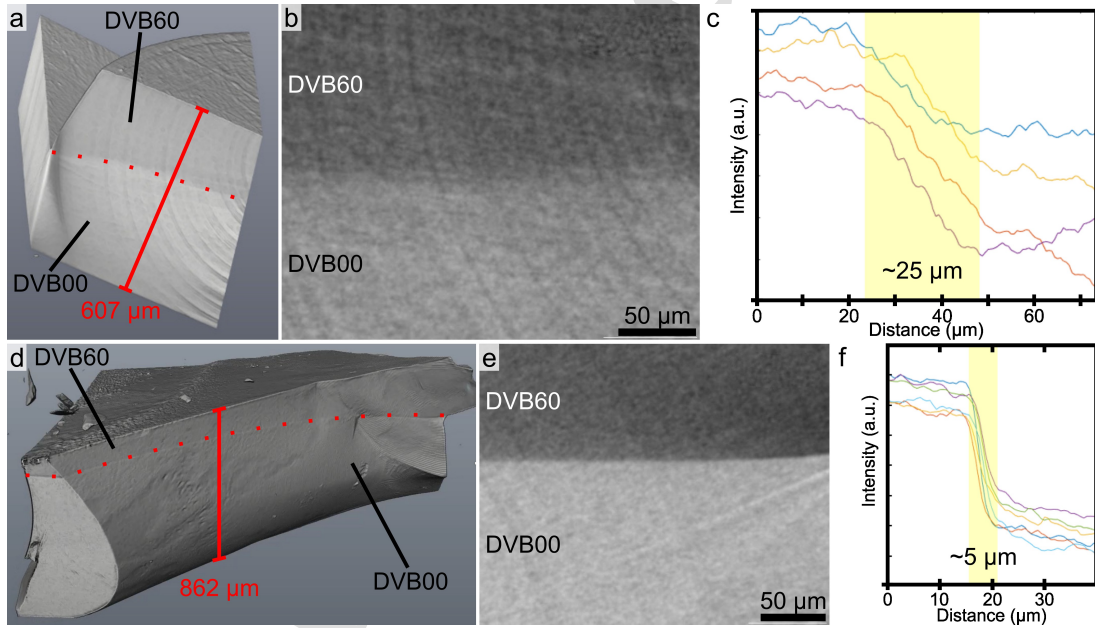

Fig. 3: Microtomography of 1400 °C pyrolyzed 60% DVB contrast bilayer SiCN and transition length determination: **a)** 3D reconstruction of a DVB60|00 piece; **b)** 2D view on interface region serving for grayscale intensity profile measurements; **c)** several intensity profiles perpendicular to the interface, featuring a transition length of ∼25 μm for DVB60|00 casting order; **d)** 3D reconstruction of a cleaved DVB00|60 piece; **e)** 2D view on interface region; **f)** several intensity profiles perpendicular to the interface, featuring a transition length of ∼5 μm for DVB00|60 casting order. Ring artifacts visible in a) and b), less expressed in d) and e).

3.3 Influence of the intermediate curing

With the objectives to facilitate electrical characterization, increase the segment lengths perpendicular to the interface, and reduce influencing factors, a set of four different types of laterally heterogeneous SiCN bars was investigated where only the degree of pre-curing from extensive to none and the casting order were varied. Types 0, 2, 4, and 5 (Table 1) were selected which were all fabricated in the same molds (11×3 mm^2), with the same DVB00/40 filling contrast, identical pyrolysis conditions (60 K/h heating rate in the critical range, 1000 °C peak temperature), and same cut triangular geometry (Figure S6f) for scanning. T0 represents the GB–L approach where the first part was solidified by extensive thermal curing before addition of the second part. On the contrary, not any intermediate curing was performed in case of T5, both dissimilar PCPs were directly pipetted in liquid state (L–L). With T2 and T4, two examples with pre-curing to slightly and significantly reduced extent were included.

The four prepared specimens, shown in Figure S5, have lengths ranging from 3.4–4.4 mm, while the microtomography setup's field of view covers only 700 µm in this dimension. Even when the top surfaces exhibited signs of an interface line as it was the case for T2 and T5 (Figure S5c,g,i,j), capturing of the interface region in a single scan remained very challenging due to its non-vertical character.

3.3.1 Short gradients with intermediate curing

The 3D reconstructed data of a T0 (DVB40|00) scan in Figure 4a i shows the smooth top surface entirely consisting of DVB00 SiCN. Below, a darker layer is clearly distinguishable with a decreasing thickness from the wider DVB40 to the narrower DVB00 end. The interface shape and orientation are a consequence of the casting process as Figure 1 illustrated previously. A closer look at the cross section reveals the presence of three distinct layers, suggesting that the cured DVB40 tip partially lifted from the PTFE mold bottom. The liquid DVB00 PCP then both filled this gap and covered the sloped top surface. The captured volume is crack-free and shows no porosity or interface delamination. The rough top surface which DVB40 typically forms was conformally adopted by the DVB00 layer above. Segmentation and partial blue coloring of the latter in Figure 4a ii bring out the rough but sharp in-

14

262 terface character in this DVB40|00 T0 sample with extensive pre-curing. While the brighter unfilled
263 layer appears homogeneous and fully dense, the generally darker DVB-filled region seems inhomoge-
264 neous. Darker features (reduced X-ray absorption due to a smaller linear attenuation coefficient) are
265 present with an increasing occurrence towards the bottom surface.

266 The same kind of low-density features was also observed in the type 2 sample where DVB-free
267 PCP was cast first and partially crosslinked during 5 min at 200 °C. They occurred exclusively in
268 the DVB40 region and are visible on the entire cross section in Figure 4b i. Segmentation and green
269 highlighting within the transparent matrix (Figure 4b ii) demonstrates their distribution and hence the
270 two-phase arrangement in 3D. The zone within the sample where the two dissimilar PCPs overlap is
271 exactly captured in the field of view of this scan. Clearly visible in this side view, the reduced extent of
272 thermal pre-curing did not significantly alter the interface characteristics. The interface line is clearly
273 defined and due to the DVB00|40 casting order smoother in this case.

274 Neither in the case of the scanned homogeneous DVB40 discs from our previous work [55] nor the
275 bilayer samples' DVB60 layers (Figure 3), such low-density features were observed before. The lab
276 scale microtomography system used for the homogeneous samples lacks both the required resolution
277 and contrast. The bilayer samples were scanned at PSI TOMCAT, for a larger field of view with the
278 10× lens compared to the 20× lens setup applied in case of the laterally heterogeneous bars. Conse-
279 quently, voxels of the bilayer sample scans were 2^3=8 times larger, therefore possibly not resolving
280 the features before. Furthermore, it is also possible that the inhomogeneity with light features only
281 occurs in DVB40 material and not in case of lower or higher DVB-filling concentrations. The mi-
282 crotomography data alone does not allow the clear identification of the low-density features. They
283 could either consist of a light solid element (e.g. graphitic carbon) or a gas (porosity). For this rea-
284 son, all four laterally arranged specimens were cleaved approximately in the middle and their cross
285 sections were inspected by SEM. The images in Figure S7 show the fracture surfaces but no evidence
286 of any porosity, suggesting fully dense character of the SiCN material. The smooth and dense T4
287 cross section (Figure S7h,i) resembles DVB00 SiCN at this position but T2 or T5 (Figure S7d-g,j-k)
288 exhibit dark features which do not appear like pores. These observations suggest that phase separa-
289 tion occurs and micrometer-sized graphitic carbon forms in DVB40-filled SiCN. This possibly results

15

²⁹⁰ from the decomposition of locally enriched polymerized DVB which did not cross-polymerize with
²⁹¹ the polysilazane.

3.3.2 Longer gradients through reduced intermediate curing

²⁹³ With decreasing extent of pre-curing, longer composition (i.e., carbon concentration) gradients are
²⁹⁴ expected. In case of the PCP-joining type 4 (DVB00 partially pre-cured during 1 min at 175 °C),
²⁹⁵ three vertically shifted microtomography scans were recorded. By stitching of the adjacent data, a
²⁹⁶ nearly 2 mm long continuous segment of the specimen was reconstructed in 3D. The grayscale image
²⁹⁷ in Figure 4c i shows a crack-free volume with a smooth top surface and rough side walls (from the
²⁹⁸ diamond wire sawing). Both the top and bottom surface exhibit aligned c-shaped grayscale contrasts,
²⁹⁹ indicated by the red arrow. In the typical concave shape of the firstly cast PCP (DVB00 in this case),
³⁰⁰ this suggests a partial material consolidation resulting from the mild pre-curing avoiding extensive
³⁰¹ mixing of the two dissimilar PCPs. In the bulk volume, the same low-density features as observed in
³⁰² the previous two cases are present. These features, which are presumably graphitic carbon again, were
³⁰³ segmented and highlighted in Figure 4c ii in green. They occurred across the entire captured specimen
³⁰⁴ length. The side view visualizes a high concentration in the direction towards the sample's DVB40
³⁰⁵ end. From right to left, the concentration decreases continuously with a noticeable drop at the position
³⁰⁶ of the superficial grayscale contrasts. At the left end of the captured volume (DVB00 direction),
³⁰⁷ almost no more low-density features are present. This example of mild pre-curing (T4) suggests that
³⁰⁸ composition contrasts in polymer-derived SiCN can be tailored to yield gradients ranging from the
³⁰⁹ submicrometer to the millimeter range, probably ~2.5 mm in this case. For an exact quantification,
³¹⁰ more scans would be required to cover an even longer part of the specimen.

³¹¹ Lastly, the liquid-liquid approach with no pre-curing was analyzed using the example of T5
³¹² (DVB40|00). The processed microtomography data from one scan is presented in Figure S8. The
³¹³ grayscale 3D images (Figure S8a-c) show typical bottom and sidewall texture and a rough top surface.
³¹⁴ Cross sections exhibit no lateral material contrast or interface but the inhomogeneously distributed
³¹⁵ dark features observed in DVB40 material before. The segmentation (yellow) in Figure S8d,e reveals
³¹⁶ predominant occurrence in proximity to the bottom and top surface which could be recently discussed

16

near-surface abnormal graphitization [45], but is also more expressed to the top left. Localization of
the captured volume on the OM images in Figure S5g,j suggests that the transition is centered a bit fur-
ther in the DVB00 direction and therefore not captured in this scan. The composition gradient in this
L-L approach is expected to be longer than in the previous T4 type, therefore no significant trend of
the low-density feature concentration could be identified within the covered range of less than 700 μm
on the DVB40 side of the interface. However, above-mentioned observations, such as the visible con-
trast in the GB state (Figure S6a) or the significant difference in both ends' electrical conductivity
in PDC state (Figure S6i and Table S1), have confirmed that there is a long-range composition- and
property-contrast also in case of type 5.
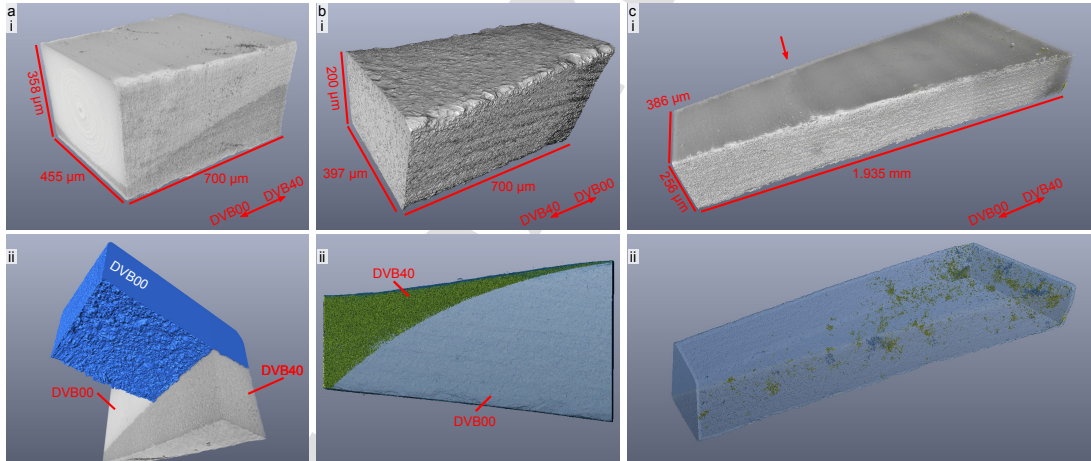
**Fig. 4: Tomographic microscopy of triangular center pieces of 1000 °C pyrolyzed laterally het-
erogeneous bars**. **a) T0:** The DVB40 PCP was cast first and extensively pre-cured before casting
of the DVB00 PCP: **i)** 3D reconstruction with smooth upside up, crack- and pore-free volume; **ii)** seg-
mentation and partial highlighting of the DVB00 layer in blue to bring out the interface roughness;
b) T2: The DVB00 PCP was cast first and shorter-time pre-cured before casting of the DVB40 PCP:
i) 3D reconstruction with upside up, crack-free volume; **ii)** volume transparency and green segmenta-
tion of single-digit μm-sized volumes with much lower density which only occur in the DVB40 region,
side view showing exactly the region where the two dissimilar PCP overlap, curved and smooth inter-
face; **c) T4:** The DVB00 PCP was cast first and pre-cured to low extent before casting of the DVB40
PCP: **i)** 3D reconstruction stitched from three scans, upside up, crack-free volume with a c-shaped
surface contrast; **ii)** volume transparency and green segmentation of single-digit μm-sized volumes
with much lower density which occur more towards the DVB40 end.

17

3.4 Proof-of-concept application

Spatially defined property contrasts, e.g. in electrical conductivity, in functionally graded ceramic parts entirely composed of SiCN allow for an integration of functionality. As a first proof-of-concept, a monolithic SiCN square plate with two cylindrical electrical feedthroughs is proposed in Figure 5a, where high carbon content areas are seamlessly integrated into an insulating matrix. Among several possible fabrication processes, a two-step molding approach with an inset PCP droplet placing and extensive pre-curing (Figure 5b,c) and reduced pyrolysis heating rate has led to intact SiCN plates of $14{\times}14{\times}0.6$ mm^3 size. Mechanically stable electrical contacts were established by a silver epoxy and an LED as a simple example of an electronic component was powered and lit up through the mono-lithic BFT SiCN plate (Figure 5d). However, further fabrication optimization and extended testing are required in order to ensure precise spatial definition of the conductive and insulating ceramic areas al-lowing for efficient and safe application. Ultimately, complexity in geometry and functionality would be increased and functionally graded all-ceramic reactor chambers or housings for electronics could be realized. Instead of the prototype visualization (an assembled BFT plate fitted into a non-ceramic case: Figure S9), two or more parts could be joined in green state by the polymer-based bonding technique and yield full ceramic bodies after pyrolysis.

4 Summary & Conclusion

In this work, the development and characterization of functionally graded polymer-derived SiCN was introduced. Based on pressureless thermal processing of the preceramic poly(methylvinylsilazane) *Durazane 1800* and the composition- and property-tuning by DVB addition, monolithic ceramic parts with engineered property-contrasts were fabricated by consecutive casting of dissimilar precursor for-mulations. DVB-filled and unfilled PCPs were joined in PTFE molds in vertical bilayer or lateral arrangement. The degree of the intermediate thermal treatment was varied, i.e., liquid precursor of one composition was combined with cured, partially cured, or liquid precursor of the dissimilar com-position. DVB-contrast green parts were transformed into carbon-contrast SiCN by pyrolysis under Ar atmosphere with peak temperatures of 1000 and 1400 °C and 60–100 K/h heating and cooling rates. Obtained ceramic parts, their phases, and the interface characteristics were analyzed by microscopy,
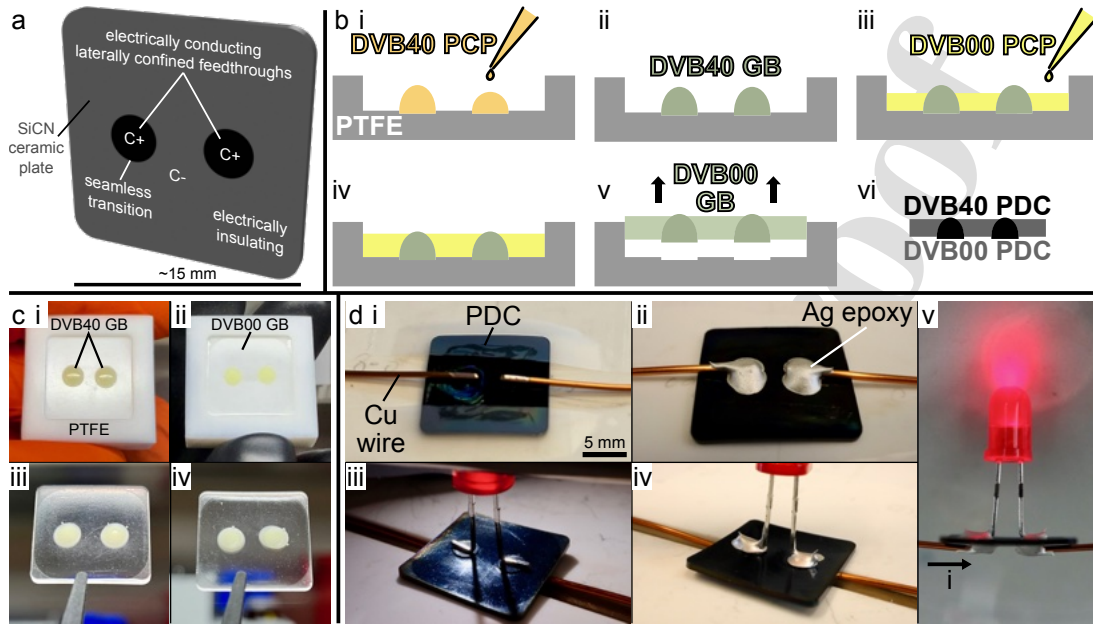
18

Fig. 5: Functionally graded bi-feedthrough SiCN plate as a usage example: **a)**: schematic concept showing the two electrical feedthroughs which exhibit locally defined higher carbon content; **b)** schematic fabrication process: **i)** inset DVB40 PCP formulation droplet placing; **ii)** thermal crosslinking of insets; **iii)** casting of the DVB00 matrix PCP; **iv)** matrix filling height slightly lower than droplet peak; **v)** removal of the crosslinked bi-material GB from the mold; **vi)** BFT-PDC plate obtained after pyrolysis; **c)** photographs of the fabrication process: **i)** two thermally cured DVB40 PCP droplet insets; **ii)** fully cured BFT plate with DVB00 matrix in PTFE mold; **iii)** upside of a demolded green state BFT plate; **iv)** bottom side of a demolded green state BFT plate; **d)** FGC demo device assembly process: **i)** positioning of Cu wires on the ceramic plate's top side feedthrough regions; **ii)** Ag epoxy applied and thermally cured for electrical contact and mechanical fixation; **iii)** positioning of the LED electrodes on the bottom side feedthrough regions; **iv)** Ag epoxy applied and thermally cured; **v)** power supplied through the ceramic lighting up the LED.

electrical conductivity measurements, EDX, TEM, and synchrotron-based tomographic microscopy.

Pore-free composition-contrast green parts were fabricated in short time by consecutive casting of the organopolysilazane-based precursor system with DCP and DVB and pressureless thermal curing at maximum temperatures of 200 °C. Low heating and cooling rates in the order of 60–100 K/h during the inert atmosphere pyrolysis have shown to be essential for the conversion to crack-free carbon-contrast PDCs. Cross-sectional microscopy and 3D microtomography have demonstrated the dense and defect-free character of millimeter-sized parts in different geometries and arrangements. The same techniques have also shown that seamless interfaces with no signs of delamination were formed irrespective of the PCP joining states. The character of the interface between ceramic regions

19

derived from unfilled PCP and PCP filled with DVB at concentrations of 40–60 wt.% was analyzed and correlated to the casting order and extent of intermediate thermal curing. If DVB-filled precursor was cast first and thermally pre-cured before being brought into contact with the unfilled liquid counterpart, partial volatilization altered the interface shape (e.g. forming curvature) which was typically rough. The inverted casting order yielded geometries more accurate to shape and smoother interface planes. The sharpest material contrast with an interface transition length below 1 µm was observed by EDX in case of the DVB60|00 bilayer arrangement with extensive intermediate curing. Several steps of longer gradients (5 µm, 25 µm, and >1.9 mm) were visualized by microtomography, resulting from varied casting order and reduced intermediate thermal curing. Even when the dissimilar PCPs were joined both in liquid state (laterally) with no intermediate curing, long range composition contrasts were obtained as electrical conductivity measurements of the monolithic SiCN material suggested. Localized differences in carbon concentration were identified in electrical conductivity contrasting samples by EDX and TEM microstructure analysis. Microtomography of C-contrast SiCN exhibited micrometer-sized low-density features in regions derived from DVB40 precursor which are probably graphitic carbon. While the liquid PDC route is well compatible with molding, shape forming of the interface requires further research with attention to gravitational and mold surface wetting influences.

Acknowledgements

Declaration of interests

The authors declare that they have no known competing financial interests or personal relationships that could have appeared to influence the work reported in this paper.

References

1. Colombo, P., Mera, G., Riedel, R. & Soraru, G. D. Polymer-derived ceramics: 40 years of research and innovation in advanced ceramics. *Journal of the American Ceramic Society* **93,** 1805–1837 (2010).

2. Wang, K., Unger, J., Torrey, J. D., Flinn, B. D. & Bordia, R. K. Corrosion resistant polymer derived ceramic composite environmental barrier coatings. *Journal of the European Ceramic Society* **34,** 3597–3606 (2014).

3. Li, N., Cao, Y., Zhao, R., Xu, Y. & An, L. Polymer-derived SiAlOC ceramic pressure sensor with potential for high-temperature application. *Sensors and Actuators A: Physical* **263,** 174–178 (2017).

4. Fernie, J. A., Drew, R. A. L. & Knowles, K. M. Joining of engineering ceramics. *International Materials Reviews* **54,** 283–331 (2009).

5. Nohut, S. & Schwentenwein, M. Vat Photopolymerization Additive Manufacturing of Functionally Graded Materials: A Review. *Journal of Manufacturing and Materials Processing* **6,** 17 (2022).

6. Marković, S., Lukić, M. J., Škapin, S. D., Stojanović, B. & Uskoković, D. Designing, fabrication and characterization of nanostructured functionally graded HAp/BCP ceramics. *Ceramics International* **41,** 2654–2667 (2015).

7. Sebastian, M. T., Wang, H. & Jantunen, H. Low temperature co-fired ceramics with ultra-low sintering temperature: A review. *Current Opinion in Solid State and Materials Science* **20,** 151–170 (2016).

8. Sebastian, M. T. & Jantunen, H. Low loss dielectric materials for LTCC applications: a review. *International Materials Reviews* **53,** 57–90 (2008).

9. Elssner, G. & Petzow, G. Metal/ceramic joining. *ISIJ International* **30,** 1011–1032 (1990).

10. Hu, K., Zhao, P., Li, J. & Lu, Z. High-resolution multiceramic additive manufacturing based on digital light processing. *Additive Manufacturing,* 102732 (2022).

11. Colombo, P., Sglavo, V., Pippel, E. & Woltersdorf, J. Joining of reaction-bonded silicon carbide using a preceramic polymer. *Journal of Materials Science* **33,** 2405–2412 (1998).

12. Lewinsohn, C. A., Colombo, P., Reimanis, I. & Ünal, Ö. Stresses Occurring during Joining of Ceramics Using Pre-ceramic Polymers. *Journal of the American Ceramic Society* **84,** 2240–2244 (2001).

13. Tang, B., Wang, M., Liu, R., Liu, J., Du, H. & Guo, A. A heat-resistant preceramic polymer with broad working temperature range for silicon carbide joining. *Journal of the European Ceramic Society* **38,** 67–74 (2018).

14. Chen, Y., Cao, Y. & Wang, Y. Electrical property of joints made of polymer-derived SiAlCN ceramic via adhesive joining. *Ceramics International* **47,** 3649–3656 (2021).

15. Duo, L., Zhang, Z., Zheng, K., Wang, D., Xu, C. & Xia, Y. Perhydropolysilazane derived SiON interfacial layer for Cu/epoxy molding compound composite. *Surface and Coatings Technology* **391,** 125703 (2020).

16. An, L., Zhang, W., Bright, V., Dunn, M. & Raj, R. Development of injectable polymer-derived ceramics for high temperature MEMS. *Proceedings IEEE 13th Annual International Conference on MEMS (Cat. No.00CH36308)* (2000).

17. Liew, L.-A., Zhang, W., Bright, V. M., An, L., Dunn, M. L. & Raj, R. Fabrication of SiCN ceramic MEMS using injectable polymer-precursor technique. *Sensors and Actuators A: Physical* **89,** 64–70 (2001).

18. Liew, L.-A., Zhang, W., An, L., Shah, S., Luo, R., Liu, Y., Cross, T., Dunna, M. L., Bright, V., Daily, J. W., Raj, R. & Anseth, K. Ceramic MEMS. *American Ceramic Society Bulletin* **80,** 25–30 (2001).

19. Flores, O., Bordia, R. K., Nestler, D., Krenkel, W. & Motz, G. Ceramic Fibers Based on SiC and SiCN Systems: Current Research, Development, and Commercial Status. *Advanced Engineering Materials* **16,** 621–636 (2014).

20. Barroso, G., Li, Q., Bordia, R. K. & Motz, G. Polymeric and ceramic silicon-based coatings – a review. *Journal of Materials Chemistry A* **7,** 1936–1963 (2019).

21. Eckel, Z. C., Zhou, C., Martin, J. H., Jacobsen, A. J., Carter, W. B. & Schaedler, T. A. Additive manufacturing of polymer-derived ceramics. *Science* **351,** 58–62 (2016).

22. Zanchetta, E., Cattaldo, M., Franchin, G., Schwentenwein, M., Homa, J., Brusatin, G. & Colombo, P. Stereolithography of SiOC Ceramic Microcomponents. *Advanced Materials* **28,** 370–376 (2016).

23. Mera, G., Riedel, R., Poli, F. & Müller, K. Carbon-rich SiCN ceramics derived from phenyl-containing poly(silylcarbodiimides). *Journal of the European Ceramic Society* **29,** 2873–2883 (2009).

24. Mera, G., Navrotsky, A., Sen, S., Kleebe, H.-J. & Riedel, R. Polymer-derived SiCN and SiOC ceramics – structure and energetics at the nanoscale. *Journal of Materials Chemistry A* **1,** 3826 (2013).

25. Greil, P. Active-Filler-Controlled Pyrolysis of Preceramic Polymers. *Journal of the American Ceramic Society* **78,** 835–848 (1995).

26. Gao, Y., Mera, G., Nguyen, H., Morita, K., Kleebe, H.-J. & Riedel, R. Processing route dramatically influencing the nanostructure of carbon-rich SiCN and SiBCN polymer-derived ceramics. Part I: Low temperature thermal transformation. *Journal of the European Ceramic Society* **32,** 1857–1866 (2012).

27. Chowdhury, M. A. R., Wang, K., Jia, Y. & Xu, C. Semiconductor-conductor transition of pristine polymer-derived ceramics SiC pyrolyzed at temperature range from 1200°C to 1800°C. *Journal of the American Ceramic Society* **103,** 2630–2642 (2019).

28. Sorarù, G. D., Tavonatti, C., Kundanati, L., Pugno, N. & Biesuz, M. Effect of the pyrolysis atmosphere on the mechanical properties of polymer-derived SiOC and SiCN. *Journal of the American Ceramic Society* (2020).

29. Santhosh, B., Ionescu, E., Andreolli, F., Biesuz, M., Reitz, A., Albert, B. & Sorarù, G. D. Effect of pyrolysis temperature on the microstructure and thermal conductivity of polymer-derived monolithic and porous SiC ceramics. *Journal of the European Ceramic Society* **41,** 1151–1162 (2021).

30. Shah, S. R. & Raj, R. Mechanical properties of a fully dense polymer derived ceramic made by a novel pressure casting process. *Acta Materialia* **50,** 4093–4103 (2002).

31. Duan, R.-G., Kuntz, J. D., Garay, J. E. & Mukherjee, A. K. Metal-like electrical conductivity in ceramic nano-composite. *Scripta Materialia* **50,** 1309–1313 (2004).

32. Makowska, M., Sasikumar, P. V. W., Hagelüken, L., Sanchez, D. F., Casati, N., Marone, F., Blugan, G., Brugger, J. & Swygenhoven, H. V. Cracks, porosity and microstructure of Ti modified polymer-derived SiOC revealed by absorption-, XRD- and XRF-contrast 2D and 3D imaging. *Acta Materialia* **198,** 134–144 (2020).

33. Ma, C., He, C., Wang, W., Yao, X., Yan, L., Hou, F., Liu, J. & Guo, A. Metal-doped polymer-derived SiOC composites with inorganic metal salt as the metal source by digital light processing 3D printing. *Virtual and Physical Prototyping,* 1–13 (2020).

34. Jeong, H.-R., Huh, T.-H., Kim, B. H. & Kwark, Y.-J. Preparation of conductive Si/C/N/Ni ceramic nanocomposites using phenyl-substituted polysilazane and nickelocene as precursors. *Ceramics International* **48,** 16576–16583 (2022).

35. Dalcanale, F., Grossenbacher, J., Blugan, G., Gullo, M. R., Lauria, A., Brugger, J., Tevaearai, H., Graule, T., Niederberger, M. & Kuebler, J. Influence of carbon enrichment on electrical conductivity and processing of polycarbosilane derived ceramic for MEMS applications. *Journal of the European Ceramic Society* **34,** 3559–3570 (2014).

36. Greenough, M., Zhao, Z., Jacobsohn, L. G., Tong, J. & Bordia, R. K. Low/intermediate temperature pyrolyzed polysiloxane derived ceramics with increased carbon for electrical applications. *Journal of the European Ceramic Society* **41,** 5882–5889 (2021).

37. Liu, G., Kaspar, J., Reinold, L. M., Graczyk-Zajac, M. & Riedel, R. Electrochemical performance of DVB-modified SiOC and SiCN polymer-derived negative electrodes for lithium-ion batteries. *Electrochimica Acta* **106,** 101–108 (2013).

38. Ma, B., Cao, Y., Gao, Y. & Wang, Y. Fabrication of a thin double-layer thermistor based on DVB-modified polymer-derived SiCN ceramics. *Journal of Alloys and Compounds* **732,** 491–497 (2018).

39. Ionescu, E., Francis, A. & Riedel, R. Dispersion assessment and studies on AC percolative conductivity in polymer-derived Si–C–N/CNT ceramic nanocomposites. *Journal of Materials Science* **44,** 2055–2062 (2009).

40. Dalcanale, F., Grossenbacher, J., Blugan, G., Gullo, M. R., Brugger, J., Tevaearai, H., Graule, T. & Kuebler, J. CNT and PDCs: A fruitful association? Study of a polycarbosilane–MWCNT composite. *Journal of the European Ceramic Society* **35,** 2215–2224 (2015).

41. Gangadhar, J., Maheshwari, A., Bordia, R. K., Kumar, C. S., Kubel, C. & Sujith, R. Role of carbon on the thermal and electrical properties of graphene- enriched silicon oxycarbides. *Ceramics International* **46,** 28156–28164 (2020).

42. Maheshwari, A., Gopikrishnan, E. P., Gangadhar, J. & Sujith, R. Highly conducting graphene dispersed silicon oxycarbide glasses. *Materials Chemistry and Physics* **239,** 121963 (2020).

43. Román-Manso, B., Moyano, J. J., Pérez-Coll, D., Belmonte, M., Miranzo, P. & Osendi, M. I. Polymer-derived ceramic/graphene oxide architected composite with high electrical conductivity and enhanced thermal resistance. *Journal of the European Ceramic Society* **38,** 2265–2271 (2018).

44. Wen, Q., Yu, Z. & Riedel, R. The fate and role of in situ formed carbon in polymer-derived ceramics. *Progress in Materials Science* **109,** 100623 (2020).

45. Wu, C., Lin, F., Pan, X., Chen, G., Zeng, Y., Xu, L., He, Y., Chen, Q., Sun, D. & Hai, Z. Abnormal Graphitization Behavior in Near-Surface/Interface Region of Polymer-Derived Ceramics. *Small,* 2206628 (2022).

46. Charan, M. S., Naik, A. K., Kota, N., Laha, T. & Roy, S. Review on developments of bulk functionally graded composite materials. *International Materials Reviews* **67,** 797–863 (2022).

47. Zeschky, J., Höfner, T., Arnold, C., Weißmann, R., Bahloul-Hourlier, D., Scheffler, M. & Greil, P. Polysilsesquioxane derived ceramic foams with gradient porosity. *Acta Materialia* **53,** 927–937 (2005).

48. Vakifahmetoglu, C., Zeydanli, D., de Mello Innocentini, M. D., dos Santos Ribeiro, F., Lasso, P. R. O. & Soraru, G. D. Gradient-Hierarchic-Aligned Porosity SiOC Ceramics. *Scientific Reports* **7** (2017).

49. Colombo, P. & Hellmann, J. R. Ceramic foams from preceramic polymers. *Materials Research Innovations* **6,** 260–272 (2002).

50. Colombo, P. Engineering porosity in polymer-derived ceramics. *Journal of the European Ceramic Society* **28,** 1389–1395 (2008).

51. Ryu, H.-Y., Wang, Q. & Raj, R. Ultrahigh-Temperature Semiconductors Made from Polymer-Derived Ceramics. *Journal of the American Ceramic Society* (2010).

52. Ryu, H.-Y. *Semiconductive behavior of and the fabrication of a p-n junction diode from amorphous polymer-derived ceramics* PhD thesis (University of Colorado, 2005).

53. Hu, Z., Meng, S., Li, J., Xie, W., Niu, J. & Zhou, Y. Continuous gradient ceramic/polymer composite for application in large temperature gradient connection by a polymer-derived ceramic route. *Composites Part A: Applied Science and Manufacturing* **132,** 105799 (2020).

54. Steinau, M., Travitzky, N., Zipperle, T. & Greil, P. in *Advances in Polymer Derived Ceramics and Composites* (eds Colombo, P., Raj, R. & Singh, M.) 61–69 (John Wiley & Sons, 2010).

55. Hagelüken, L., Sasikumar, P. V. W., Lee, H.-Y., di Stadio, D., Chandorkar, Y., Rottmar, M., Maniura-Weber, K., Blugan, G. & Brugger, J. Multiscale 2D/3D microshaping and property tuning of polymer-derived SiCN ceramics. *Journal of the European Ceramic Society* **42,** 1963–1970 (2022).

56. Lovric, G., Mokso, R., Schlepütz, C. M. & Stampanoni, M. A multi-purpose imaging endstation for high-resolution micrometer-scaled sub-second tomography. *Physica Medica* **32,** 1771–1778 (2016).

57. Marone, F. & Stampanoni, M. Regridding reconstruction algorithm for real-time tomographic imaging. *Journal of Synchrotron Radiation* **19,** 1029–1037 (2012).

58. Janakiraman, N. & Aldinger, F. Fabrication and characterization of fully dense Si–C–N ceramics from a poly(ureamethylvinyl)silazane precursor. *Journal of the European Ceramic Society* **29,** 163–173 (2009).

59. Mera, G. & Ionescu, E. Silicon-Containing Preceramic Polymers. *Encyclopedia of Polymer Science and Technology* (2013).

Credit Author Statement

L.H. and J.B. conceived the idea and designed the experiments. L.H. fabricated the samples. L.H., M.M. and F.M. performed characterizations. All authors discussed and analyzed the results. L.H. wrote the manuscript and all authors commented on the manuscript. All authors have given approval to the final version of the manuscript.

Declaration of interests

The authors declare that they have no known competing financial interests or personal relationships ☒
.that could have appeared to influence the work reported in this paper

The authors declare the following financial interests/personal relationships which may be considered ☐
:as potential competing interests